Large depth-of-field ultra-compact microscope by progressive optimization and deep learning

Yuanlong Zhang[1,3,4,5*], Jiachen Xie[1,3,4,5*], Xiaofei Song[9*], Jing Hu[6*], Jiawei Chen[7], Xiang Li[7], Haiyu Zhang[7], Qiqun Zhou[7], Lekang Yuan[8], Chui Kong[10], Yibing Shen[6], Jiamin Wu[1,3,4,5‡], Lu Fang[2‡], and Qionghai Dai[1,3,4,5‡]

[1] Department of Automation, Tsinghua University, Beijing 100084, China
[2] Department of Electronic Engineering, Tsinghua University, Beijing 100084, China
[3] Institute for Brain and Cognitive Sciences, Tsinghua University, Beijing 100084, China
[4] Beijing Key Laboratory of Multi-dimension & Multi-scale Computational Photography (MMCP), Tsinghua University, Beijing 100084, China
[5] Beijing Laboratory of Brain and Cognitive Intelligence, Beijing Municipal Education Commission, Beijing 100084, China
[6] State Key Laboratory of Modern Optical Instrumentation, Zhejiang University, Hangzhou 310027, China
[7] OPPO Research Institute, Shenzhen 518101, China
[8] Tsinghua-Berkeley Shenzhen Institute, Tsinghua University, Shenzhen 518055, China
[9] Tsinghua Shenzhen International Graduate School, Tsinghua University, Shenzhen 518055, China
[10] School of Information Science and Technology, Fudan University, Shanghai 200433, China

[*] These authors contributed equally to this work
[‡] Correspondence should be addressed to J.W. (wujiamin@tsinghua.edu.cn), L.F. (fanglu@tsinghua.edu.cn), and Q.D. (qhdai@tsinghua.edu.cn)

Supplementary Information Table

Supplementary Figure 1	Aspherical lens system effectively reduces the system length with high performance.
Supplementary Figure 2	Evaluation diagrams of the optical design of the proposed integrated microscope.
Supplementary Figure 3	Forward model for the generation of synthetic dataset.
Supplementary Figure 4	Comparisons between the synthetic coded images and the experimental coded images.
Supplementary Figure 5	Simulation-supervision network effectively recovers coded images.
Supplementary Figure 6	Shift-variant deconvolution algorithm outperforms uniform deconvolution algorithm.
Supplementary Figure 7	Comparisons of refocusing method with simulation-supervision method in the integrated microscope.
Supplementary Figure 8	Comparisons of unsupervised method with simulation-supervision method in the integrated microscope
Supplementary Figure 9	Spatially nonuniform PSF calibrations across a large FOV of the integrated microscope.
Supplementary Figure 10	Pruned network has comparable fidelity to unpruned network with reduced computational costs.
Supplementary Figure 11	Comparisons of conventional microscope and the proposed EDOF integrated microscope equipped on a cell phone.
Supplementary Table 1	Comparisons of the proposed integrated microscope with other miniaturized microscopes.
Supplementary Table 2	Full prescription data of the proposed integrated microscope.

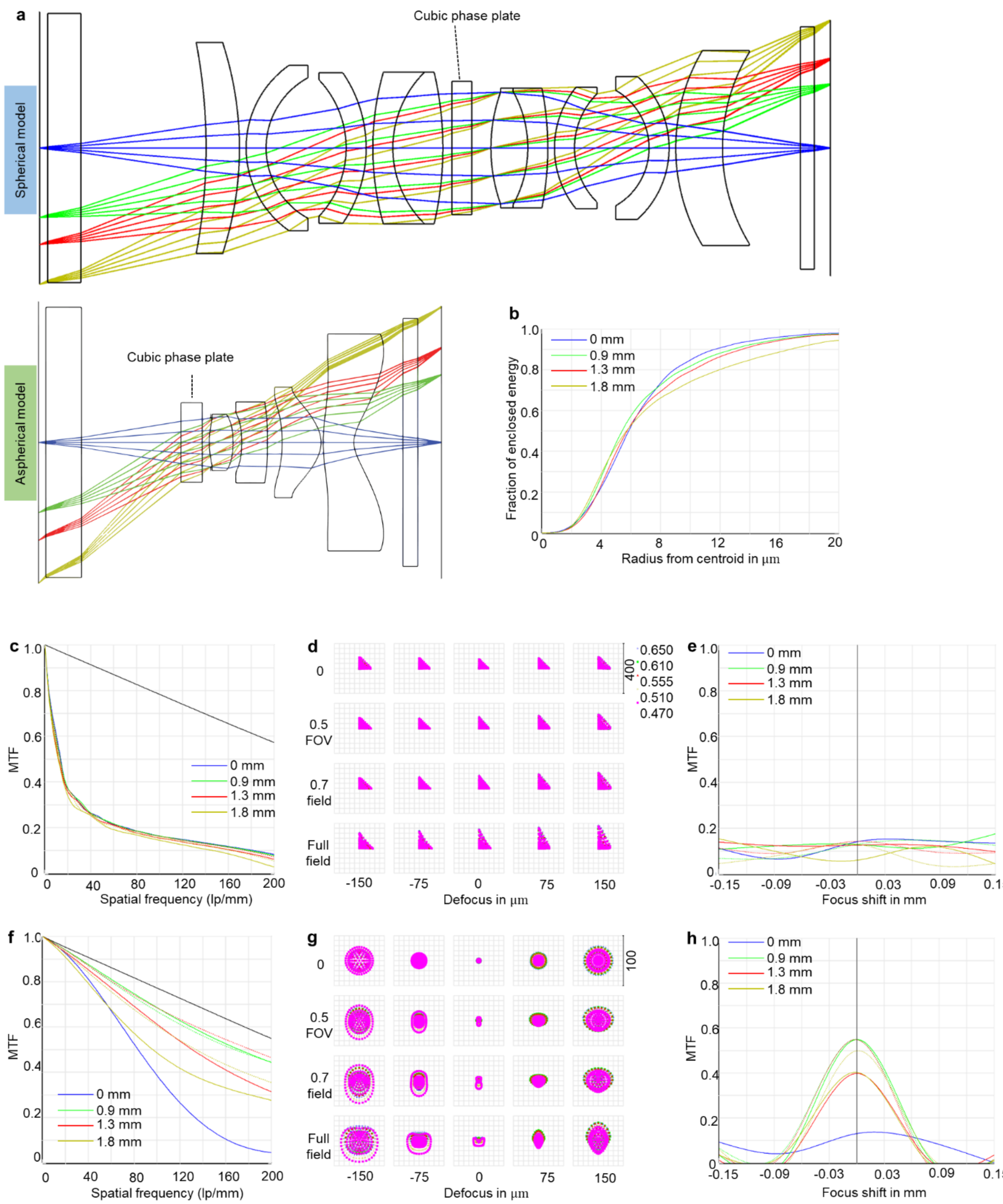

Supplementary Fig. 1. Aspherical lens system effectively reduces the system length with high performance.

a. The proposed optical design with aspherical plastic lenses (bottom) significantly reduces the size and weight of the system with spherical lenses (top) when the performance of both is similar. The conjugate distance (11.735 mm) of the spherical lens system is twice that of the aspherical lens system.

b. Encircled energy analysis of the optimized spherical system at different lateral positions of the FOV.

c-**e**. Evaluation diagrams of the spherical system with a cubic phase plate (CPP) inserted. The evaluations include modulation transfer function (MTF) at different lateral positions (**c**), spot diagram at different focal planes and different lateral positions (**d**), and the MTF along different focal planes at different lateral positions (**e**).

g-**i**. The diagrams corresponding to (**c**-**e**) without the CPP inserted in the optimized spherical system.

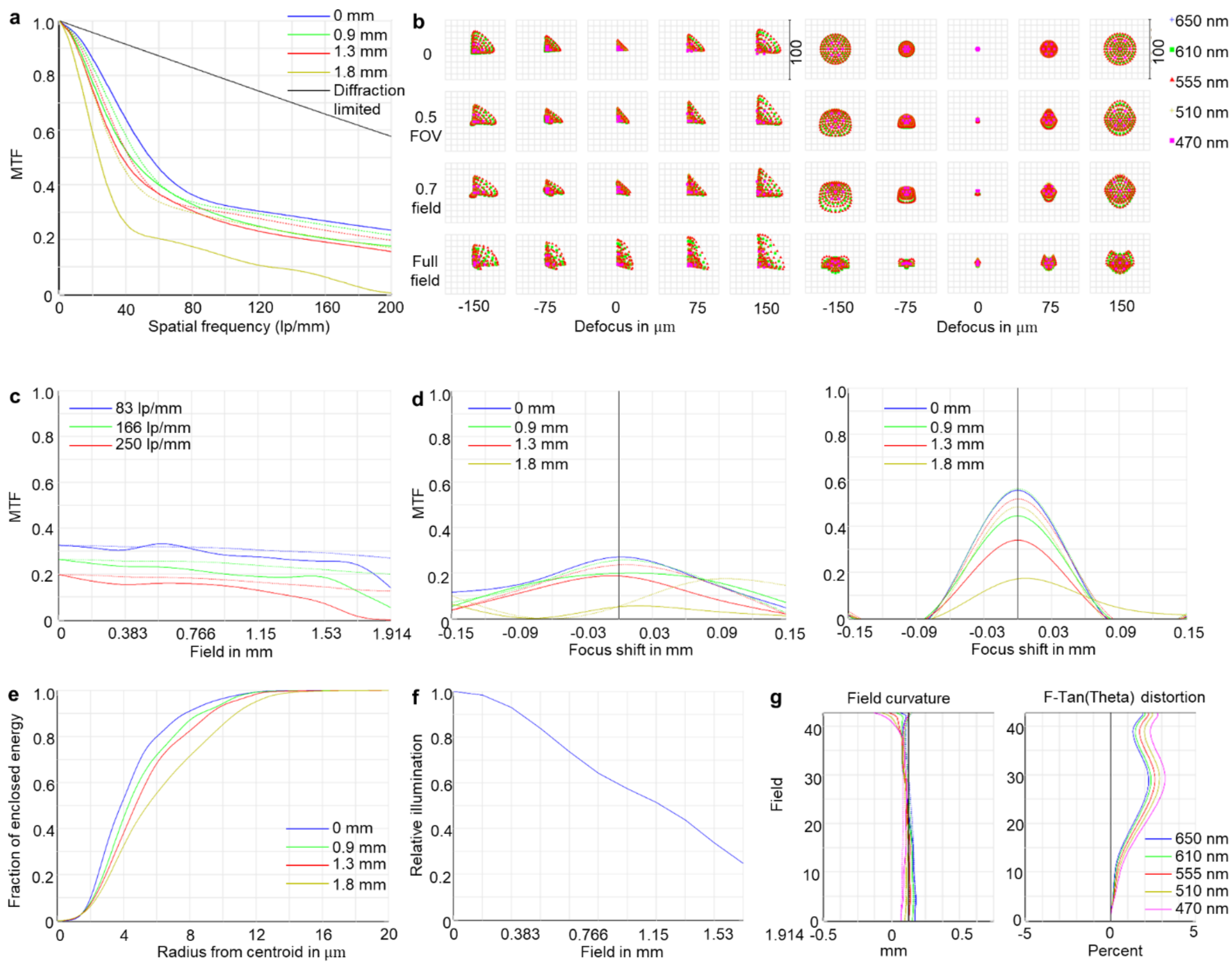

Supplementary Fig. 2. Evaluation diagrams of the optical design of the proposed integrated microscope.

a. The MTF curves across different spatial frequencies for different lateral field positions. The black solid line indicates the diffraction limit.

b. Spot diagrams at different focal planes and lateral positions for the same design with CPP (left)and without CPP (right). Different color corresponds to different wavelengths.

c. MTF across different field positions at spatial frequencies of 83, 166 and 250 lp/mm (corresponding to spatial resolution of 6 µm (blue lines), 3 µm (green lines) and 2 µm (red lines).

d. MTF at different focal planes with a spatial frequency of 166 lp/mm for the same design with CPP (left) and without CPP (right).

e. Diffraction Encircled energy across different field radius.

f. Relative illumination intensity across different field positions.

g. Field curvature and distortion across different field positions of different wavelengths.

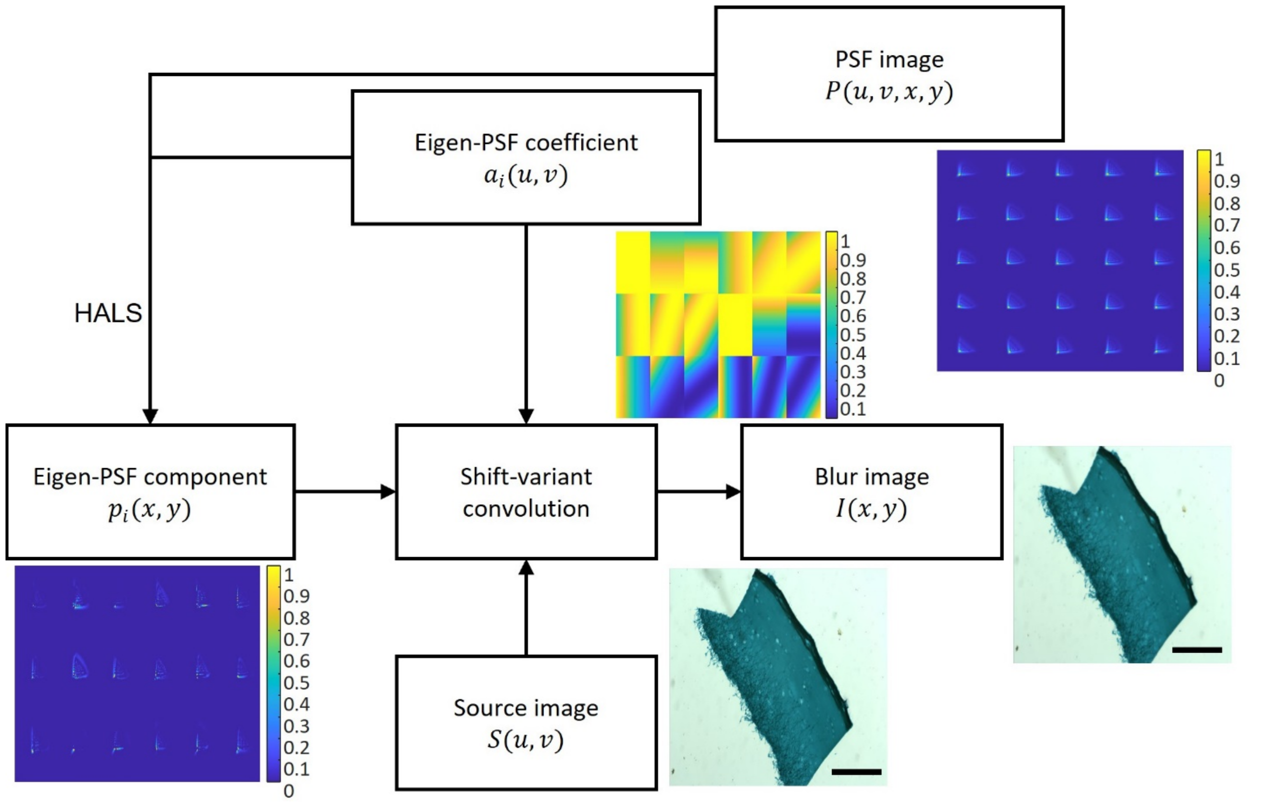

Supplementary Fig. 3. Forward model for the generation of synthetic dataset.

We consider the PSFs of our optical system as the sum of a set of orthogonal bases $p_i(x,y)$ multiplexed with the corresponding coefficient map $a_i(u,v)$ for encoding the spatial variability. Given the spatial variant PSF $P(u,v,x,y)$ simulated from large fields, we generate the eigen-PSF component $p_i(x,y)$ and corresponding coefficient $a_i(u,v)$ utilizing modified Hierarchical Alternating Least Squares (HALS) algorithm. We share the same coefficient map $a_i(u,v)$ for different color channels to suppress chromatic aberration during image reconstruction. Finally, we use shift-variant convolution formula to produce source and blur image pairs (Methods). Scale bar: 500 µm.

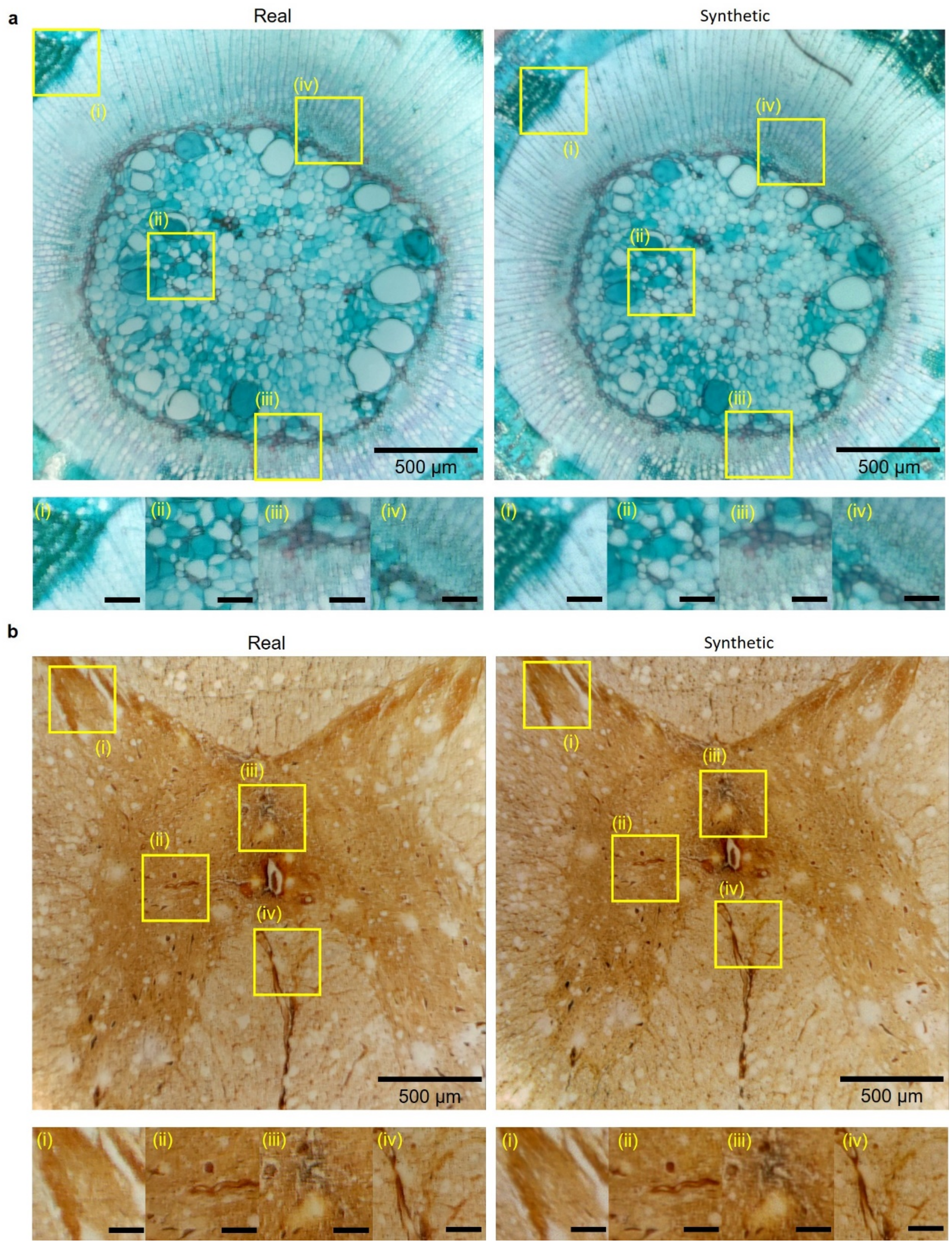

Supplementary Fig. 4. Comparisons between the synthetic coded images and the experimental coded images.
a, b. Two different samples (woody dicot stem cross section and spinal cord transection, respectively) are shown to demonstrate the similarity between the experimental data (left, scale bar: 500 µm) and the synthetic data (right, scale bar: 500 µm). Zoom-in areas from (i) to (iv) are listed in the bottom for more detailed comparisons (scale bar: 100 µm).

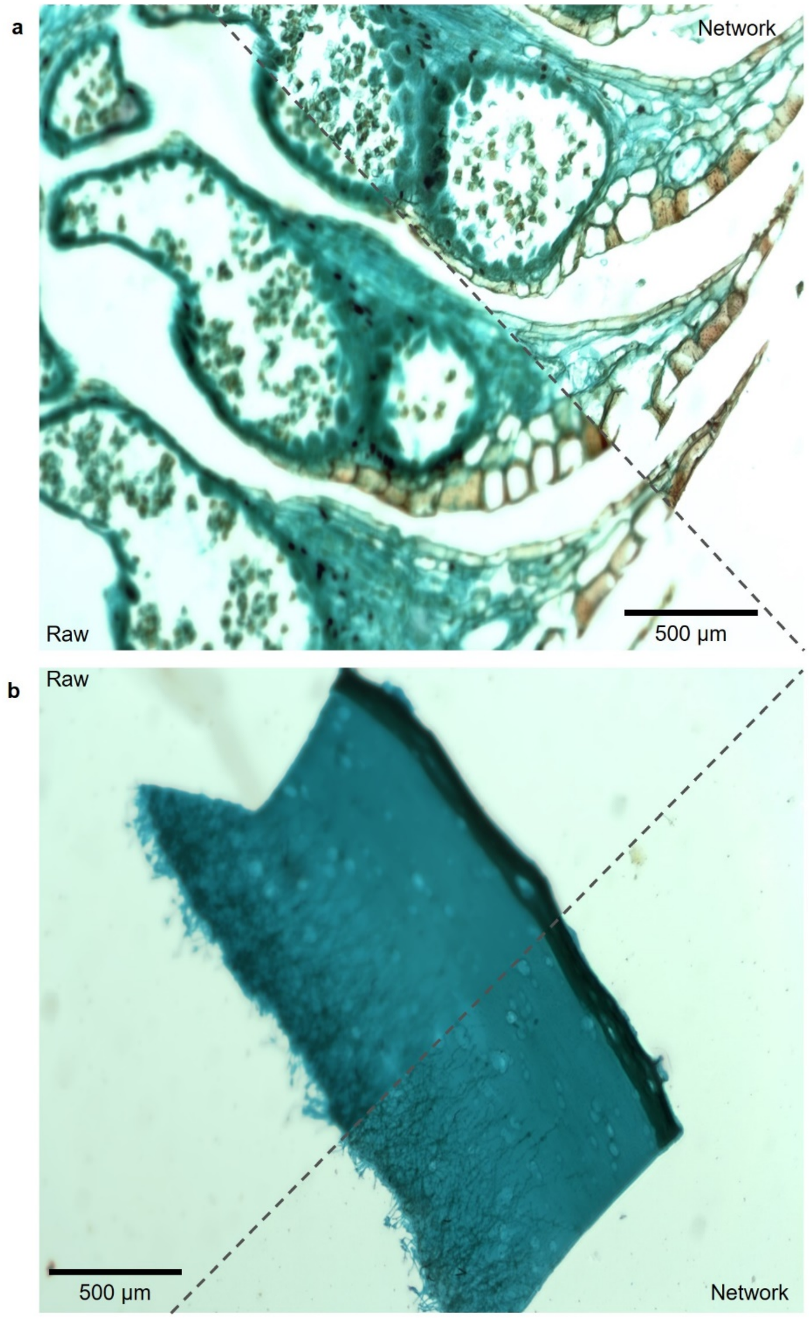

Supplementary Fig. 5. Simulation-supervision network effectively recovers coded images.

a, b. Two different sliced samples (top: pine male globose fruit, bottom: Penicillium, respectively) are displayed to indicate simulation-supervision network obviously gains clearer reconstructions from the raw images (scale bar: 500 µm).

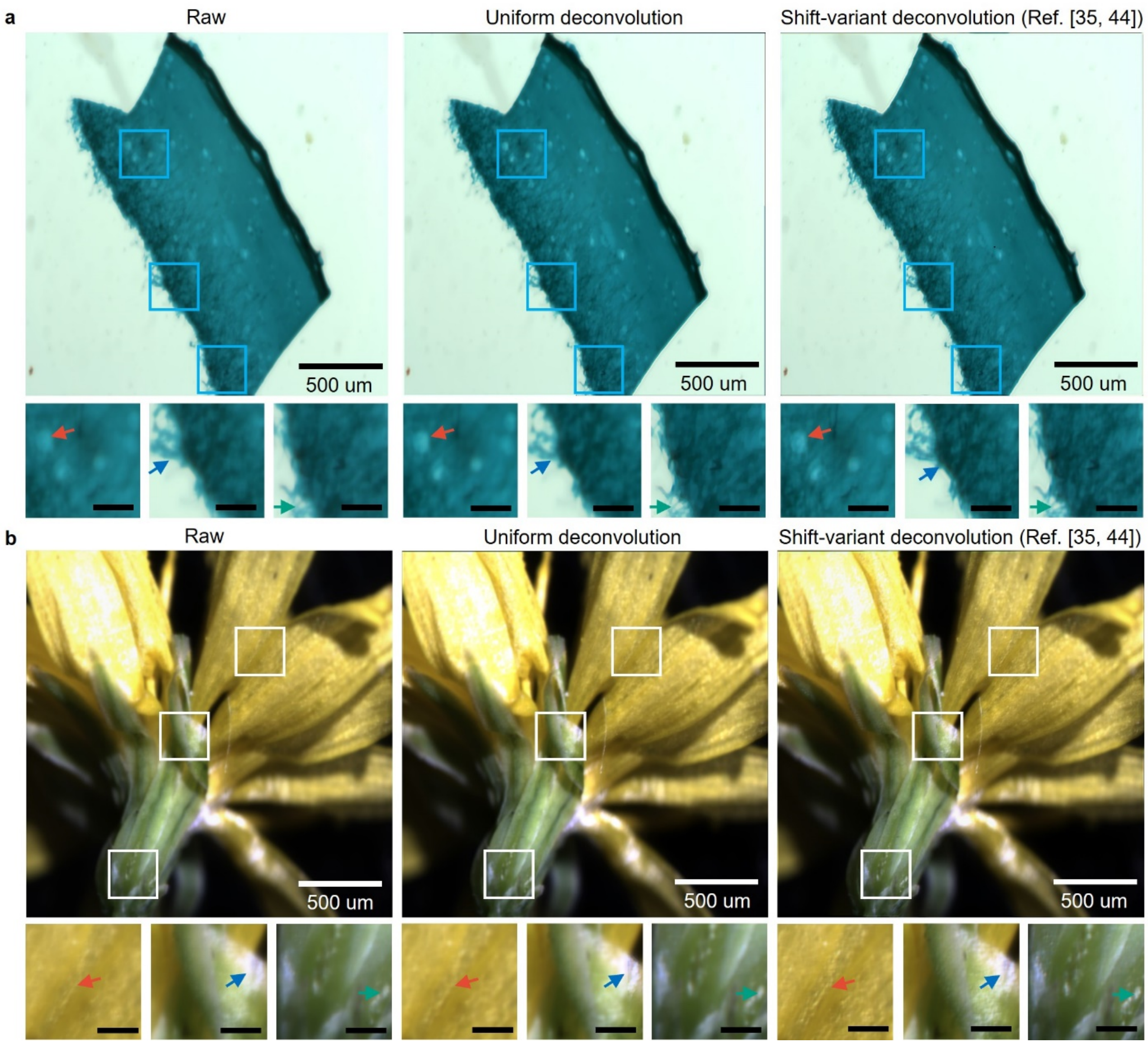

Supplementary Fig. 6. Shift-variant deconvolution algorithm outperforms uniform deconvolution algorithm. **a, b**. Two kinds of samples (Penicillium and flower, respectively) are shown to demonstrate performance comparisons of restored images obtained by uniform (middle, scale bar: 500 µm) and shift-variant deconvolution (Ref. [35, 44], right, scale bar: 500 µm) from blur images (left, scale bar: 500 µm). Zoom-in areas are listed in the bottom for further comparisons (scale bar: 100 µm), and red, blue, and green arrows show three typical features (scale bar: 100 µm), where shift-variant deconvolution achieves clearer restorations than uniform deconvolution.

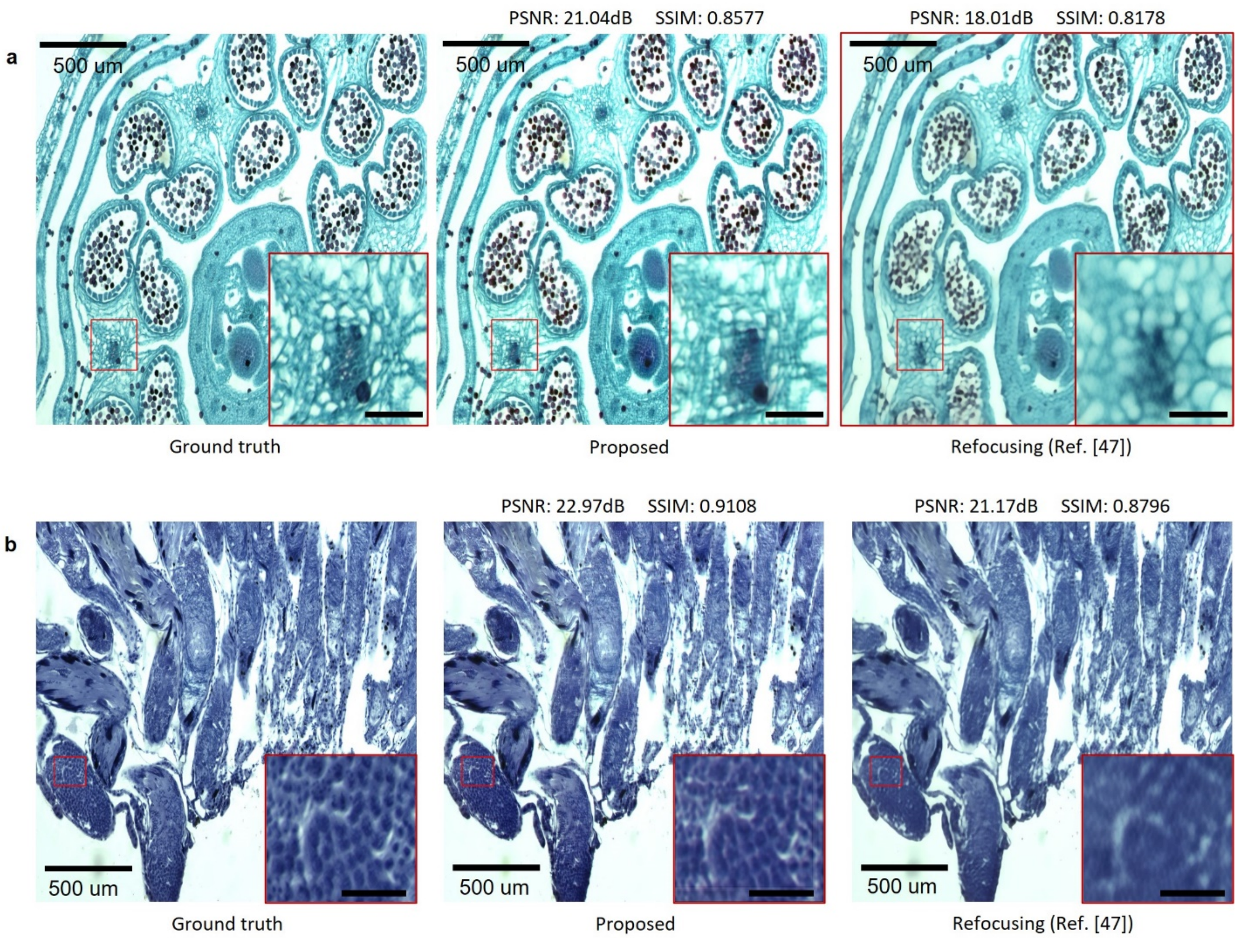

Supplementary Fig. 7. Comparisons of refocusing method with simulation-supervision method in the integrated microscope.

a, b. Two samples (rape bud and meiosis of locust testis, respectively) are presented to illustrate capability contradistinctions of recovered images acquired by simulation-supervision method (middle, scale bar: 500 μm) and refocusing method (Ref. [47], right, scale bar: 500 μm) compared to the ground truth (left, scale bar: 500 μm). Zoom-in areas (scale bar: 100 μm) are listed in the bottom right of each complete image, where proposed simulation-supervision maintains sharper restorations and more effective image quality metrics (PSNR and SSIM) than refocusing method.

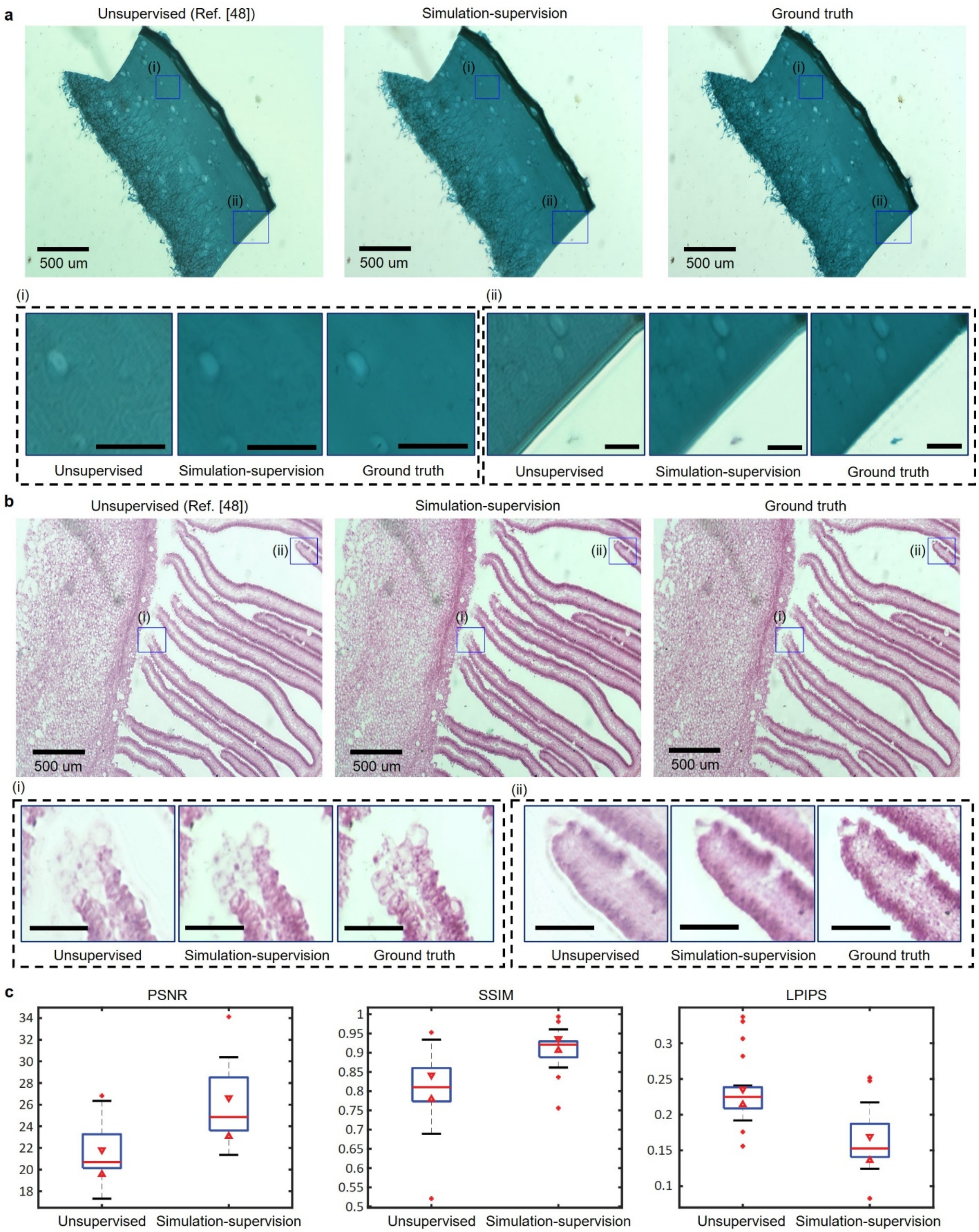

Supplementary Fig. 8. Comparisons of unsupervised method with simulation-supervision method in the integrated microscope.

a, **b**. Restoration of test samples (Penicillium and Agaricus, respectively). We test a cycleGAN model (Ref. [48]) which does not need paired training data. On the basis of the ground truth (right, scale bar: 500 µm) we find our simulation-supervision approach (middle, scale bar: 500 µm) has higher fidelity and less boundary artifacts compared to unsupervised approach (left, scale bar: 500 µm). Two sub-characteristics (i) and (ii) are extracted to be magnified and listed inside the dashed box below for further comparisons (scale bar: 100 µm).

c. Statistical comparisons of the restoration quality between the unsupervised method and proposed simulation-supervised network on 145 samples in terms of PSNR (left), SSIM (middle), and perceptual loss (LPIPS, right).

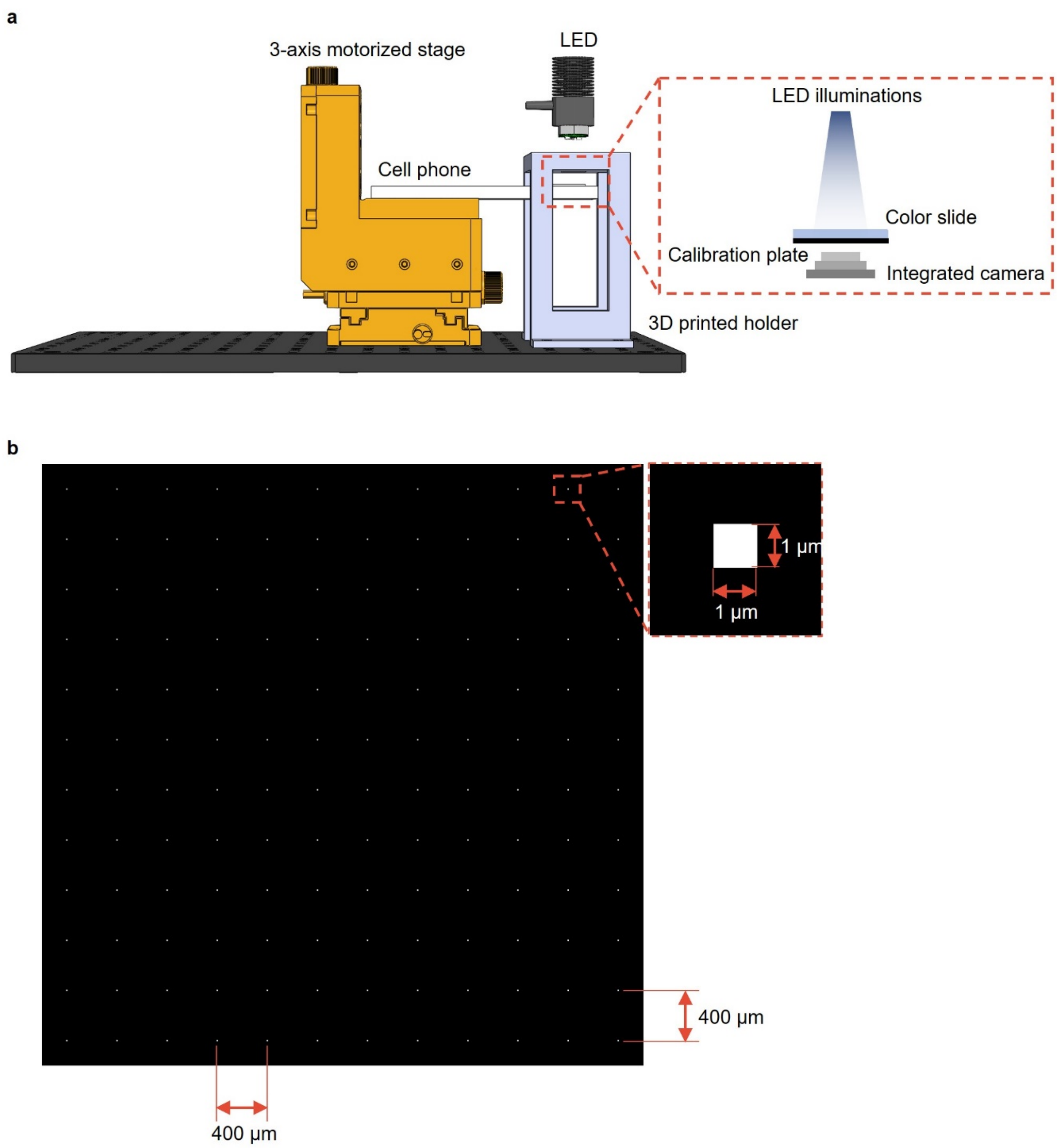

Supplementary Fig. 9. Spatially nonuniform PSF calibrations across a large FOV of the integrated microscope.

a. A sketch of PSF calibration setup, which consists of a 3-axis motorized stage, a LED source, a 3D printed holder, and an integration camera (assembled in a cell phone). The red dashed box illustrates that the LED illumination beams are firstly uniformed by a plastic color slide, then pass through the dot array and collected by the integrated camera. The motorized stage can carry the integrated camera to realize 3D calibrations.

b. A sketch of fabricated dot array by lithography. The separation distance between adjacent dots is 400 μm, and each dot is 1 x 1 $μm^2$. The black part will block the light and the white part is transparent.

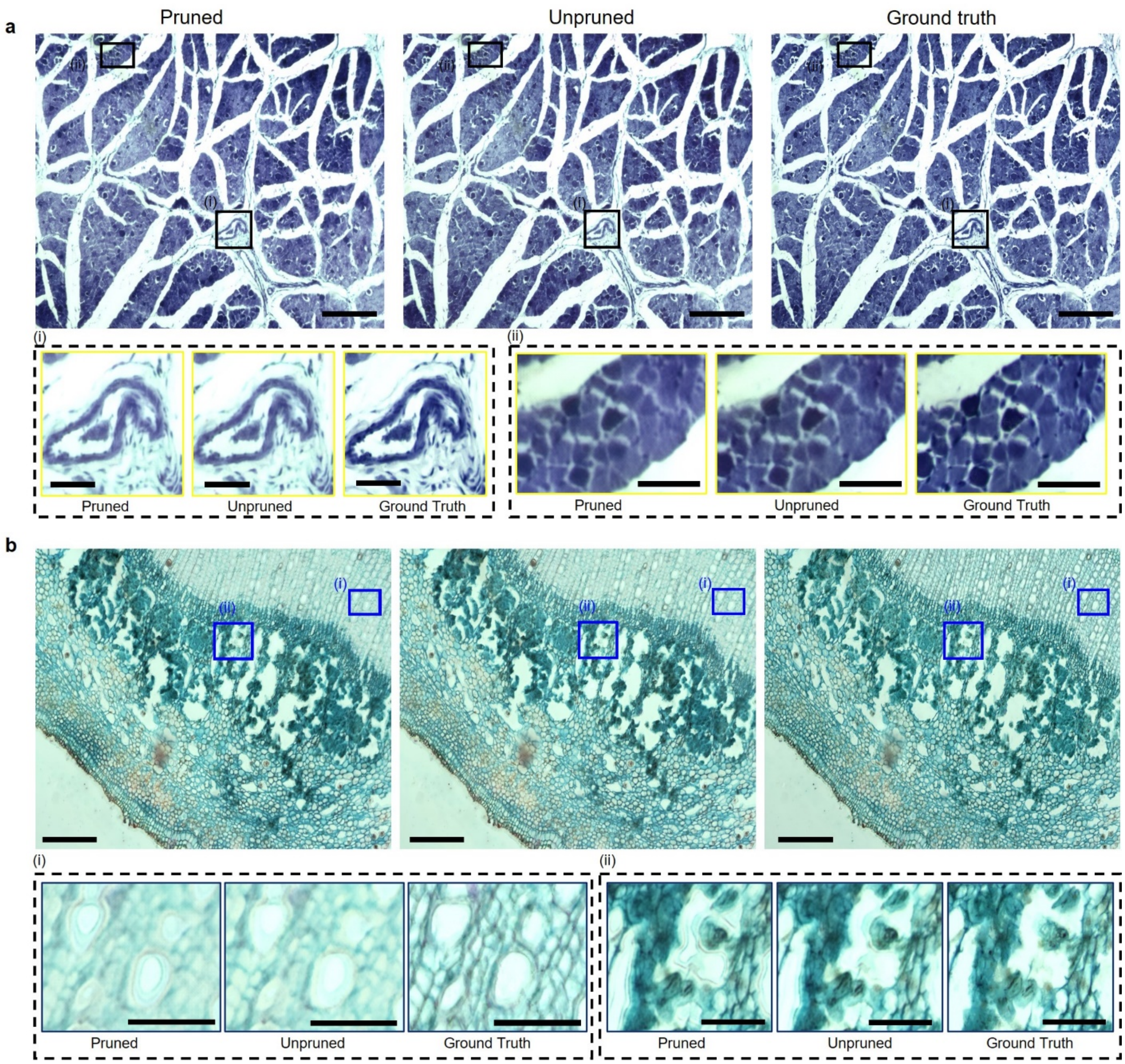

Supplementary Fig. 10. Pruned network has comparable fidelity to unpruned network with reduced computational costs.

a, **b**. Restoration of test samples (skeletal muscle and oleander stem, respectively) with pruned neural network (left, scale bar: 500 µm) and unpruned neural network (middle, scale bar: 500 µm). We find pruned neural network keeps high fidelity compared to unpruned approach in accordance with the ground truth (right, scale bar: 500 µm). Two sub-features (i) and (ii) are extracted to be enlarged and listed inside the dashed box below for further comparisons (scale bar: 100 µm).

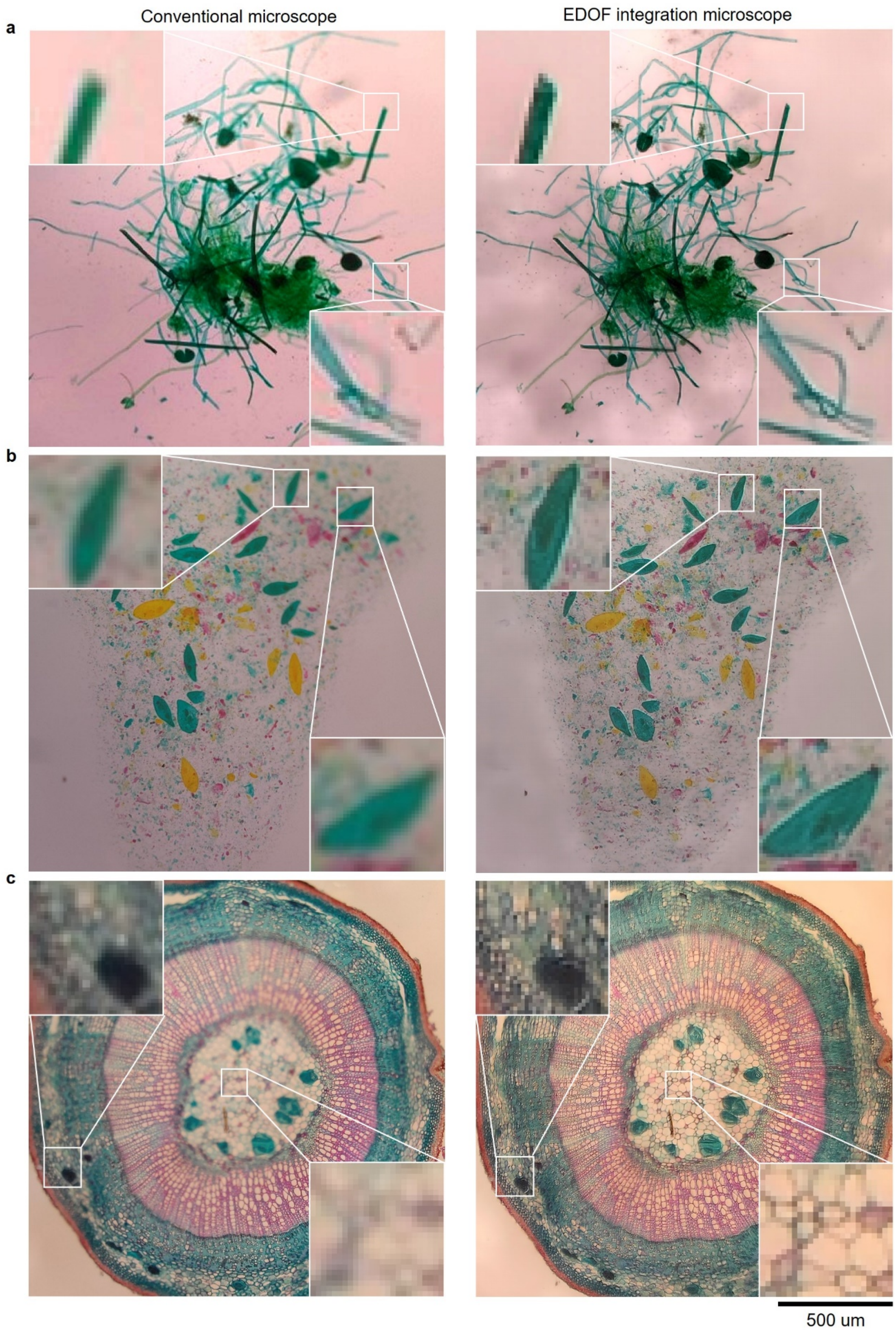

a
b
c
Conventional microscope
EDOF integration microscope
500 um

Supplementary Fig. 11. Comparisons of conventional microscope and the proposed integrated microscope equipped on a cell phone.

a, **b**, **c.** are restorations of Rhizopus nigricans, Paramecia, and root samples, respectively. Those slices are tilted to show that the proposed integrated microscope (right, scale bar: 500 µm) achieves better resolution than the conventional microscope (left, scale bar: 500 µm) in defocus areas. The zoom-in insets show the finer structural information difference of samples between two microscopes.

Supplementary Table 1. Comparisons of the proposed integrated microscope with other miniaturized microscopes.

The comparisons include weight, volume, resolution, field of view, and depth of field.

	Miniscope v3	Miniscope v4	MiniLFOV	Miniscope3D	Minifast	Mesoscope	Featherscope	Ours
Weight	3.2 gram	2.6 gram	13.9 gram	2.5 gram	3.45 gram	4.5 gram	1.0 gram	0.5 gram
Volume	~17mm x13mm x23mm	~13mm x 13mm x 22mm	~35mm x 20mm x 35mm	~17 mm x13mm x23mm	~17mm x13mm x23mm	~17 mm x 36 mm x 9 mm	~6mm x 15mm x 15mm	~5mm x 5mm x 6mm
Resolution	~1.6 µm	~2 µm	~3 µm	2.76 µm	1.5 µm	~ 5 µm	~4 µm	3 µm
Field of view	0.7mm x0.5mm	~ Φ1 mm	3.1mm x2.3mm	~0.9mm x0.7mm	0.7mm x0.5mm	~4 mm x 3 mm	~1.0 x 1.0 mm	Φ3.6 mm
Depth of field	~15 µm	~25 µm	~25 µm	~390 µm	~15 µm	~40 µm	~40 µm	~300 µm
Reference	Ref. [25]	[1]	Ref. [34]	Ref. [35]	Ref. [36]	Ref. [37]	Ref. [38]	

Supplementary Table 2. Full prescription data of the proposed integrated microscope.

Type	Radius	Thickness	Glass	Semi-diameter	Surface parameters
Standard	Infinity	0.300	EP-9000	0.566	
Extended polynomial	Infinity	0.120		0.447	Norm radius: 1.000 X3Y0: 0.030 X0Y3: 0.030
Standard (Stop)	Infinity	-0.020		0.348	
Even asphere	1.159	0.334	ZEONEX_K22R&K26R_2017	0.349	4^{th} order: -0.154 6^{th} order: 0.609 8^{th} order: -190.180 10^{th} order: 3984.058 12^{th} order: -4.469E+04 14^{th} order: 2.500E+05 16^{th} order: -5.709E+05
Even asphere	-1.503	0.122		0.401	4^{th} order: -2.588 6^{th} order: 11.561 8^{th} order: -93.332 10^{th} order: 407.060 12^{th} order: -2738.190 14^{th} order: 1.621E+04 16^{th} order: -3.887E+04
Even asphere	-2.043	0.362	EP-9000	0.425	4^{th} order: -2.226 6^{th} order: 12.109 8^{th} order: -131.037 10^{th} order: 830.923 12^{th} order: -2926.059 14^{th} order: 7570.232 16^{th} order: -1.089E+04
Even asphere	-62.219	0.207		0.574	4^{th} order: -0.753 6^{th} order: 2.469 8^{th} order: -9.494 10^{th} order: 40.041 12^{th} order: -167.800 14^{th} order: 489.624 16^{th} order: -527.432
Even asphere	-2.485	0.549	ZEONEX_K22R&K26R_2017	0.675	4^{th} order: -1.130 6^{th} order: 4.629 8^{th} order: -17.808 10^{th} order: 58.248 12^{th} order: -133.519 14^{th} order: 200.192 16^{th} order: -135.291
Even asphere	-0.414	0.030		0.781	4^{th} order: -1.389 6^{th} order: 5.524 8^{th} order: -18.141 10^{th} order: 40.662 12^{th} order: -50.310 14^{th} order: 37.270 16^{th} order: -14.720

Even asphere	2.334	0.432	ZEONEX_K22R& K26R_2017	1.168	4th order: -0.143 6th order: -0.699 8th order: 2.040 10th order: -2.769 12th order: 2.030 14th order: -0.767 16th order: 0.114
Even asphere	0.364	0.690		1.532	4th order: -0.266 6th order: 0.281 8th order: -0.215 10th order: 0.104 12th order: -0.032 14th order: 6.048E-03 16th order: -5.759E-04
Standard	Infinity	0.210	BK7	1.694	
Standard	Infinity	0.333		1.770	
Standard (Image)	Infinity			1.971	

Reference

1. http://miniscope.org/index.php/Miniscope_V4